

To appear in ApJS.

# The BATSE Gamma-Ray Burst Spectral Catalog. I. High Time Resolution Spectroscopy of Bright Bursts using High Energy Resolution Data

R. D. Preece, M. S. Briggs, R. S. Mallozzi, G. N. Pendleton, and W. S. Paciesas  
Dept. of Physics, University of Alabama in Huntsville, Huntsville, AL 35899

and

D. L. Band

Center for Astrophysics and Space Sciences, Code 0424, University of California at San  
Diego, La Jolla, CA 92093

## ABSTRACT

This is the first in a series of gamma-ray burst spectroscopy catalogs from the Burst And Transient Source Experiment (BATSE) on the *Compton Gamma Ray Observatory*, each covering a different aspect of burst phenomenology. In this paper, we present time-sequences of spectral fit parameters for 156 bursts selected for either their high peak flux or fluence. All bursts have at least eight spectra in excess of  $45\sigma$  above background and span burst durations from 1.66 to 278 s. Individual spectral accumulations are typically 128 ms long at the peak of the brightest events, but can be as short as 16 ms, depending on the type of data selected. We have used mostly high energy resolution data from the Large Area Detectors, covering an energy range of typically 28 – 1800 keV. The spectral model chosen is from a small empirically-determined set of functions, such as the well-known ‘GRB’ function, that best fits the time-averaged burst spectra. Thus, there are generally three spectral shape parameters available for each of the 5500 total spectra: a low-energy power-law index, a characteristic break energy and possibly a high-energy power-law index. We present the distributions of the observed sets of these parameters and comment on their implications. The complete set of data that accompanies this paper is necessarily large, and thus is archived electronically at: <http://www.journals.uchicago.edu/ApJ/journal/>.

*Subject headings:* gamma rays: bursts

## 1. Introduction

Gamma-ray bursts (GRBs) have recently attracted considerable attention in the literature with the realization that burst sources are most likely associated with galaxies at cosmological distances. With the observation of GRB afterglows at many different wavelengths, there is an emerging picture of what happens *after* a burst is over. It is still unclear what, exactly, the burst is. For this reason, comprehensive studies of burst properties are necessary. We present here a spectroscopy catalog, complete as of Sept. 23, 1998, describing the high time-resolution spectral behavior of bright bursts as observed with the Burst And Transient Source Experiment (BATSE) on board the *Compton Gamma Ray Observatory*.

Some results based upon these data have been reported elsewhere (Liang & Kargatis 1996, Crider et al. 1997, Preece et al. 1998a, Preece et al. 1998b). The first use of these data was to determine the low-energy behavior in peak outbursts in some GRBs as a function not of time, but of the integrated photon fluence (Liang & Kargatis 1996). This work was subsequently expanded upon (Crider et al. 1997), in support of a saturated synchrotron self-Compton emission model for bursts. A detailed study of the temporal behavior of the high-energy power-law index made heavy use of spectral fit data for a large subset of the bursts from the catalog presented here (Preece et al. 1998a). It was discovered that although bursts evolve from hard to soft in the high-energy power law as they do in the other spectral parameters (Ford et al. 1995), this evolution is not directly correlated with that of any other parameter. Finally, the entire set of spectral fits has been used to rule out the synchrotron shock model as the emission mechanism for  $\sim 30\%$  of all bursts, by a direct comparison between the observed distribution of the low-energy power-law indices with the predicted limiting value of  $-2/3$  (Preece et al. 1998b).

In this *Paper*, we bring together references to many aspects of the BATSE burst spectral observations that have heretofore been scattered throughout the literature. In the next section, we describe the two instruments that make up BATSE: the Large Area Detectors (LADs) and the Spectroscopy Detectors (SDs). In addition, the energy calibration procedures and their limitations are discussed. In §3, the methodology employed to produce this catalog is explained. This includes event and data type selection as well as the spectral models used. The format of the catalog dataset is covered in detail in §4. Finally, in §5 we discuss some of the results that can be obtained using these data, by presenting the distributions of the fitted spectral shape parameters for the entire set of spectra. These can be a valuable tool for determining the validity of proposed physical emission models. As this catalog represents a very high level of data reduction, it is our hope that the data files that accompany this paper will be a valuable resource to the entire burst community.

## 2. The BATSE Instrument

### 2.1. Overview

BATSE was conceived of primarily as an all-sky gamma-ray transient monitor. For this reason, it consists of eight separate NaI-based detector modules located on all corners of the *Compton Observatory* spacecraft; four are on the ‘top’, as defined by the placement and fields of view of the pointed gamma-ray instruments COMPTEL and EGRET, and four are on the bottom. To achieve the purpose of gathering information for the largest possible set of bursts, the LADs are constructed as a large, thin, flat collection area ( $2000 \text{ cm}^2 \times 1.27 \text{ cm}$ ) with roughly a cosine angular response. To ensure maximal sky coverage for all eight detectors, the flat faces of the detectors are oriented parallel to the faces of a octahedron. The independent detectors’ response is what allows for localization of bursting sources on the sky with an accuracy of  $\sim 2^\circ$  (Briggs et al. 1999a).

The SDs were added to BATSE when a separate instrument for this purpose was not selected for inclusion on the *Compton Observatory*. They are smaller and thicker ( $127 \text{ cm}^2 \times 7.2 \text{ cm}$ ) than the LADs to maximize photon capture and energy resolution and thus have a more uniform angular response. Only at very low energies (5 to 15 keV) is the angular response more like a cosine, due to a circular beryllium window on the face of each SD. Each of the 8 BATSE modules consists of one LAD and one SD. The principal axis of each SD is offset in angle from the normal vector to the face of the associated LAD by  $18^\circ.5$ . The direction of the SD offset angle relative to the associated LAD is toward the midplane of the spacecraft, away from the axis defined by the two *Compton* pointed instruments.

### 2.2. Energy Coverage

As a result of their different purposes, the two types of detectors have different energy capabilities. The LADs are most useful if the energy range they observe is constant over time. This conforms to their design for long-term monitoring of transient gamma-ray sources. Thus, they have been gain-stabilized throughout the mission. The nominal energy coverage is 25 to 1800 keV, with some small variations between the detectors. For the purpose of triggering on burst-like events, the pulse heights of detected counts are divided into four broad channels by on-board fast discriminators. These are roughly 25 – 50, 50 – 100, 100 – 300, and  $> 300$  keV. The on-board trigger can consist of any combination of these four channels in three timescales: 64, 256 and 1024 ms, but for the majority of the mission, the channel 2 + 3, or 50 – 300 keV, triggers has been used, since this combination is empirically found to be optimal for GRBs. It is an open question whether the burst

samples obtained under different trigger criteria have differing spectral properties (Lloyd & Petrosian 1999, Harris & Share 1998).

For LAD spectroscopy studies, the shaped pulse corresponding to the detection of a specific photon energy loss in the instrument is accumulated into one of 128 quasi-logarithmic energy-loss channels (created from 2752 linear channels) by the on-board pulse-height analyzer (PHA), according to the pulse intensity. Given the moderate energy resolution of the LADs (an average of 19.6% at 511 keV), this division oversamples the energy coverage. An energy resolution element can be defined to be equal to the FWHM of the detector energy resolution at a given energy. The typical energy range of the LADs is spanned by twenty energy resolution elements. The PHA output can be further rebinned into 16 channels according to a lookup table that is configured from the ground. Typically, the lookup table is constructed to sample the PHA output at roughly the detector resolution, resulting in the medium energy resolution of the MER/CONT data types (see below). However, at various points in the mission there was a need to observe one of several soft transient events at a higher resolution in the low-energy channels, so the table was modified accordingly. This is important for burst studies in that the energy sampling may contribute to the uncertainty in fitted spectral parameters when such data are used. No matter what the data type, a few of the lowest channels are not useful for spectroscopy, as they sample pulse heights that fall below the lower-level discriminator (LLD), an electronic cut-off that eliminates noise-produced counts.

For the SDs, all data are binned into 256 quasi-linear PHA channels. The lowest four of these, which would ordinarily contain residual noise counts from below the LLD, are replaced by data that serve the same purpose as the four LAD discriminators but have a much broader energy coverage, starting from one-half the LLD energy. The SD discriminator data are also available on a 2048 ms timescale. Unlike the LADs that have constant energy coverage over time, the SDs are separately configurable by several ground-commanded flight software parameters that have changed over time. The LLD setting determines the lowest usable PHA channel and the photo-multiplier tube (PMT) voltage sets the gain, or mapping, between PHA channels and energies of counts recorded in each channel. The higher the PMT voltages, the lower the energy coverage will be at any given LLD setting. The ‘nominal’ (1×) gain setting places the 511 keV annihilation feature in background spectra at linear PHA channel #100 (the gain response is roughly linear). In this scale, a 4× gain setting nearly matches the energy coverage of the LADs. With low LLD and high gain (8×), the SD energy threshold is at  $\sim 10$  KeV. The BATSE instrumental response functions are averaged over detector azimuth angle (Pendleton et al. 1995). The missing azimuthal dependence becomes significant when the zenith angle exceeds about 60°, so we restrict our analysis to cases with smaller angles.

### 2.3. Energy Calibration and Instrumental Response

The energy calibration of the two different BATSE detectors has been described elsewhere (Preece et al. 1998a, Band et al. 1992). Residual non-linearities in the SD PHA output renders the first ten channels above the LLD unusable, although in many cases, there may be overlapping coverage from other detectors that may observe the same event. This omission stills allows for roughly two decades of coverage in each detector, which can be extended with the inclusion of the SD discriminator data below the LLD (Preece et al. 1996), although we have not done this in the present catalog. The relative calibration between energy-integrated spectra for the LADs and the SDs has an apparent offset of about 10%, partly due to the modelling of an aluminum honeycomb support structure for the LAD charged-particle detectors as a solid sheet of aluminum with an equivalent mass-thickness in the LAD response function. Work is now in progress to address this issue; however, the relative calibration becomes most important in joint fits of data from each detector type, which also have not been done here. In addition, if there were a method for determining the distance to each source from the flux, the absolute calibration (determining the difference between the observed flux and a standard reference, such as the Crab, for example) would be crucial. Currently, only a few bursts have had their red-shifts measured, although this will likely improve in the future.

The description of the BATSE detector response matrices was presented by Pendleton et al. (1995), while Briggs (1995) reviewed the role of the detector characteristics in the forward-folding technique. Of interest in the current work is the nature of the off-diagonal contributions. The direct response ('photopeak') comes from photoelectric absorption of photons that interact in the body of the detector. Beside the photopeak, there is a large contribution generated by the iodine K-shell photon cross-section edge at  $\sim 33$  keV. The lower cross-section below the K-shell ionization energy allows some photons to escape the detector. If the escaping photon is the X-ray florescence product of the photoelectric absorption of a higher-energy photon, a lower total energy will be recorded for the original photon. This effect can be seen in Figure 1 as a broad second peak in the response that diverges from the photopeak at low energies. As this feature is imposed on the response by physics, it can serve as a convenient marker in energy, to aid in calibration of the gain. Photons that scatter into the detector from various sources, including the detector housing, the spacecraft, and the Earth's atmosphere, as well as those that Compton scatter out of the detector, make a broad lower-diagonal contribution from the higher energy external photons. These effects can be best seen in the counts predicted for photons of a single energy interacting with the detector, as in Figure 2 for the background spectral line features at 68,  $\sim 200$ , and 511 keV. The various components of the response have differing energy dependencies that change with the viewing angles from the detector to the source and the

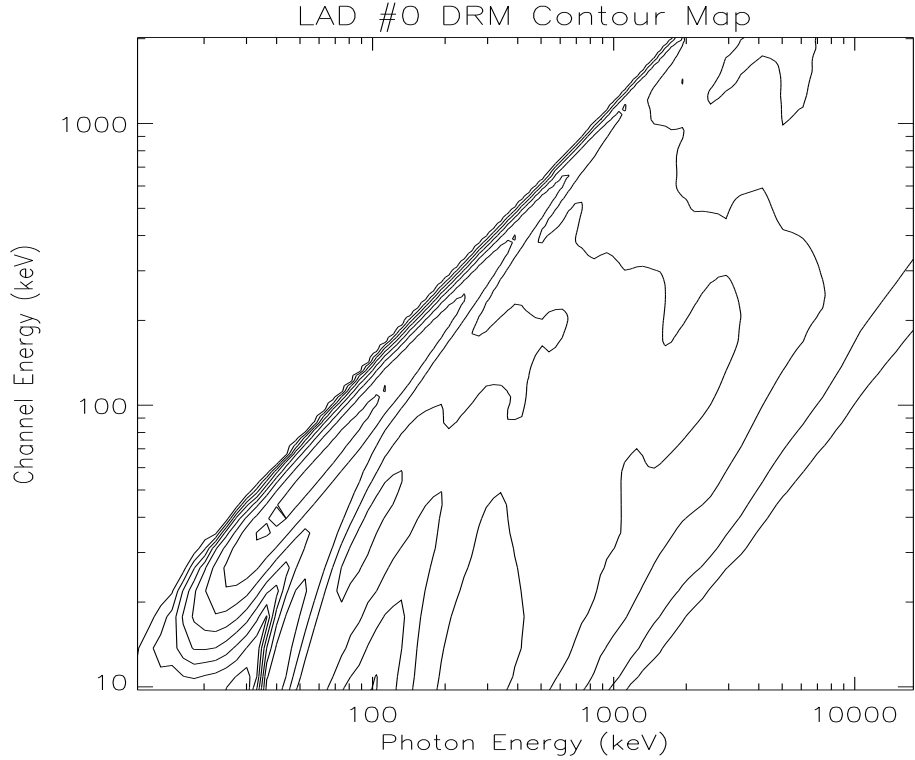


Fig. 1.— A typical BATSE LAD response matrix with equal levels of effective area indicated by 8 logarithmically-spaced contour lines, between 0 and the maximum of  $63 \text{ cm}^2 \text{ keV}^{-1}$ . The response to a photon of any given energy incident upon the detector can be traced by a vertical slice through the contour map at that energy. The photopeak is visible along the diagonal, while the iodine K-escape feature shows up along the bottom at 33 keV.

Earth. Deconvolution of the count spectra becomes an exercise in the redistribution of the observed counts according to an assumed photon model; it is not unique.

The spacecraft flies in a roughly circular, inclined, and low-Earth orbit that creates a time- and energy-dependent background environment. In most cases, this background varies smoothly with time, so the separation of source and background counts is straightforward. However, there are a number of low-energy transient sources that contribute a considerable amount of noise when they are active, such as Sco X-1, the Vela pulsar and especially Cygnus X-1, that can emit weak, soft, flickering pulses at times of intense outburst. Such sources are most difficult for the SD data spectral analyses, as they are typically softer than the LAD energy bandpass, so they are not a concern here, except for those cases where SD data alone were available.

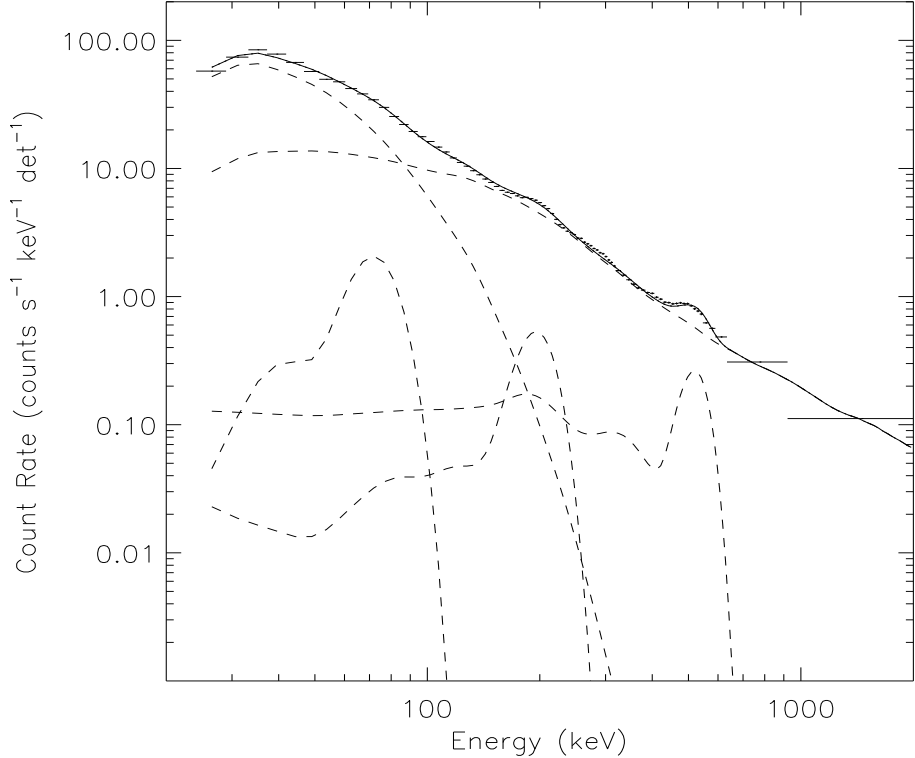


Fig. 2.— Fitted typical HER background spectrum for TJD 10459 from 34536.2 to 34831.1 s UT, showing five components (*dashed*). The model includes a low-energy ‘thermal’ portion, plus a  $\sim -1$  spectral index high-energy power law and background lines at 511 keV,  $\sim 200$  keV and 68 keV. The data are fit using these photon models propagated through the detector response matrix shown in Fig. 1. Note that some of the background continuum counts are due to particles, not gamma-ray photons.

### 3. Methodology

#### 3.1. Burst Selection Method

In order to obtain a reasonable time-resolved picture of the spectral evolution in individual bursts, we consider bright bursts only in this catalog. We chose bursts to analyze using peak flux and total fluence limits, where these were determined by the methods described in the BATSE burst catalogs (Fishman et al. 1994, Meegan et al. 1996, Paciesas et al. 1999). By selecting bursts that satisfied either one of these criteria, we take maximum advantage of the time-to-spill spectral accumulation for the PHA data. For example, bursts with large peak flux may not have a large enough total fluence to be included in the sample by that criterion alone, but may still have a considerable number of spectra with

sufficient counts to be useful for spectroscopic analysis. The total fluence selection criterion is  $4 \times 10^{-5}$  erg cm $^{-2}$  integrated over all energies ( $> 20$  keV). For peak flux, the catalog value must exceed 10 ph cm $^{-2}$  s $^{-1}$  on the 1024 ms integration timescale in the BATSE trigger energy band (50 – 300 keV). Bursts were selected that had at least one of these catalog values available, to avoid any bias.

The total duration of burst emission is selected by human judgement, usually starting with the first spectrum after the trigger, since for bright events, only unusual circumstances will allow any significant emission to be undetected before the trigger. Once the selection has been made, the spectra are rebinned in time according to a signal-to-noise ratio (S/N) criterion, in order to have a sufficient count rate in each spectrum so that the spectral model parameters could be determined with reasonable accuracy. To determine the S/N, the integrated background-subtracted count spectrum is compared with the total uncertainty, so the resulting measure is in units of standard uncertainty ( $\sigma$ ). For LAD spectra over their total usable energy range, our minimum acceptable S/N was chosen to be 45, or roughly  $2\sigma$  per energy resolution element (discussed above) in a hypothetical flat LAD count spectrum. For most bright bursts, the peak spectra have count rates that are well in excess of  $45\sigma$ , so it is typically the quiescent periods between peaks where spectra are binned together in this manner. SD data were used in some unusual cases where the LAD data were missing or unacceptable due to the presence of electronic distortions from overly high count rates. For these data, the S/N used to rebin the spectra in time was 15. Any bin at the end of the burst selection interval is likely to have less than  $45\sigma$ , so it is dropped. We rejected bursts that had less than eight spectra total after the rebinnning to ensure that enough spectra were available to track spectral evolution through each burst. After all the criteria have been applied to the entire BATSE data set from the beginning of the mission until Sept. 23, 1998, 156 bursts are available for this catalog.

General information about the selected bursts is presented in Table 1. Each burst is identified by the BATSE catalog name and trigger number (columns 1 & 2), and several global properties are given that characterize each event, such as the number of spectra fit (column 6), the time interval chosen for fitting (7), and the peak flux and total fluence (8 & 9) from the spectral fits. These last two values may differ from those in the official BATSE burst catalogs; the most important difference in the peak flux values is that there is no common time interval over which all of them are determined, since they depend upon the time-to-spill intervals in the spectral data. As such, they are given here as a rough guide of relative intensity. Indeed, the peak flux distribution (Figure 3) suffers from the bias of selecting bursts based upon total fluence or peak flux, rather than peak flux alone, as can be seen by the deficit in low peak flux bursts below 20 photons s $^{-1}$  cm $^{-2}$ . The fluences have been calculated by integrating the individual spectral model fits over the total fitted energy

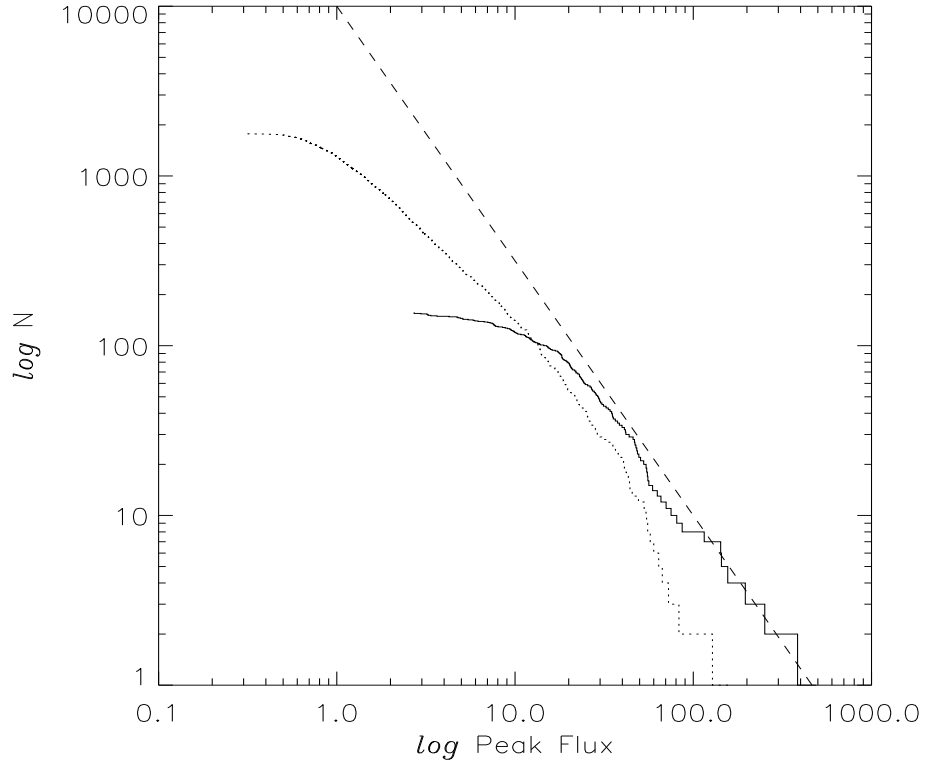


Fig. 3.— Peak flux distribution for the catalog bursts, compared with a  $-3/2$  power law (dashed) as well as the 1772 BATSE 64 ms peak flux catalog values for the same period of time (dotted - the ‘Current’ catalog: <http://www.batse.msfc.nasa.gov/batse/>). It is important to note that this set of bright bursts has an obvious selection bias, since they were selected on the basis of their total fluence or peak flux. In addition, there are peak fluxes based upon a 16 ms timescale included in our sample, so some values are brighter than they would be in the BATSE 64 ms peak flux data set.

range (typically 25 – 1800 keV for LAD data) and summing over all spectra (as binned) in the time interval selected, which generally differs from the interval chosen for the BATSE burst catalog fluences. By using the best-fit model for each spectrum, this value represents a fair estimate of the fluence, at least for the  $> 45\sigma$  portion of the burst history. The uncertainties associated with these two values were omitted for clarity and may be found in the online version of the catalog. The other columns of Table 1 refer to specifics of the data and spectral model selection, and will be described below.

Table 1. General Characteristics of Catalog Bursts.

Burst Name <sup>a</sup> (1)	Trigger Number (2)	Data Type (3)	Detector Number <sup>b</sup> (4)	Model Used <sup>c</sup> (5)	No. of Spectra (6)	Time Interval (s) Start (7) Stop	Peak Flux <sup>d</sup> (ph cm <sup>-2</sup> s <sup>-1</sup> ) (8)	Fluence <sup>d</sup> (erg cm <sup>-2</sup> ) (9)
3B 910421	105	HERB	7	GRB	14	0.064	10.304	27.6
3B 910425	109	CONT	4	GRB	14	-16.384	53.248	4.7
3B 910503	143	HERB	6	GRB	27	0.704	4.800	142.7
3B 910522	219	MER	456	BPL	51	105.499	135.963	33.1
3B 910601	249	HERB	2	GRB	15	0.0	17.856	28.1
3B 910619	394	HERB	1	GRB	34	0.0	44.480	7.6
3B 910627	451	HERB	4	GRB	16	0.0	11.968	21.9
3B 910717	543	HERB	4	GRB	10	0.0	6.144	16.4
3B 910807	647	HERB	0	BPL	23	0.0	28.288	10.2
3B 910814C	676	HERB	2	GRB	18	0.0	54.592	7.8
3B 910814	678	HERB	2	BPL	37	0.0	29.376	22.9
3B 911031 <sup>†</sup>	973	HERB	3	GRB	37	0.0	33.728	12.1
3B 911118 <sup>†</sup>	1085	HERB	4	BPL	50	0.0	13.696	49.0
3B 911126	1121	HERB	4	GRB	28	18.688	29.888	19.7
3B 911127	1122	HERB	1	GRB	36	0.0	28.672	18.3
3B 911202	1141	HERB	7	GRB	31	0.064	17.856	22.1
3B 911209	1157	HERB	1	GRB	18	0.128	23.360	19.1
3B 920210	1385	HERB	5	BPL	35	0.0	48.768	7.5
3B 920226 <sup>†</sup>	1440	HERB	3	GRB	16	9.728	17.920	20.4
3B 920311	1473	HERB	5	GRB	51	3.392	23.168	46.5
3B 920315	1484	HERB	3	BPL	8	0.0	20.096	20.7
3B 920406	1541	SHERB	2	GRB	20	61.120	87.232	41.5
3B 920513	1606	CONT	3	GRB	28	12.288	102.400	9.3
3B 920525	1625	HERB	4	GRB	35	4.160	19.712	54.6
3B 920622 <sup>†</sup>	1663	HERB	4	GRB	60	0.0	24.384	39.0
3B 920627	1676	SHERB	2	GRB	29	0.064	38.080	12.4
3B 920711	1695	HERB	7	SBPL	28	0.0	36.288	35.9
3B 920718	1709	HERB	7	GRB	13	0.128	5.056	29.3
3B 920723	1721	HERB	3	BPL	32	0.064	30.464	14.0
3B 920902	1886	HERB	5	GRB	30	0.064	14.592	29.5
3B 921003	1974	HERB	2	GRB	21	0.0	9.536	13.2
3B 921009	1983	HERB	2	GRB	54	0.064	29.184	34.6
3B 921015	1989	CONT	4	BPL	31	110.592	350.208	6.0
3B 921022	1997	HERB	2	GRB	22	0.0	45.824	9.9
3B 921118	2061	HERB	4	BPL	16	0.0	50.560	3.2
3B 921123	2067	HERB	1	GRB	44	12.160	31.744	29.8
3B 921207 <sup>†</sup>	2083	HERB	0	GRB	36	0.0	14.336	88.3
3B 921209	2090	HERB	1	GRB	17	0.0	13.888	15.8
3B 921230	2110	MER	57	COMP	29	-2.048	31.774	7.5
3B 930106	2122	HERB	6	GRB	12	0.064	73.856	2.7
3B 930120	2138	MER	012	SBPL	125	66.715	111.515	17.3
3B 930201	2156	MER	137	SBPL	250	-3.072	173.056	37.2
3B 930405	2286	HERB	6	GRB	26	0.0	25.152	15.4
3B 930425	2316	HERB	1	GRB	33	0.0	29.440	7.6
3B 930506	2329	HERB	3	GRB	26	0.0	13.888	73.5
3B 930916	2533	HERB	3	GRB	43	0.0	39.488	13.7
3B 930922	2537	HERB	1	GRB	23	0.064	4.864	67.3
3B 931008	2571	MER	236	BPL	43	0.030	163.870	7.8
3B 931026	2606	CONT	7	GRB	18	11.264	97.280	3.8
3B 931103	2617	HERB	5	GRB	23	0.064	18.688	15.2

Table 1—Continued

Burst Name <sup>a</sup> (1)	Trigger Number (2)	Data Type (3)	Detector Number <sup>b</sup> (4)	Model Used <sup>c</sup> (5)	No. of Spectra (6)	Time Interval (s) Start (7)	Stop (7)	Peak Flux <sup>d</sup> (ph cm <sup>-2</sup> s <sup>-1</sup> ) (8)	Fluence <sup>d</sup> (erg cm <sup>-2</sup> ) (9)
3B 931126	2661	HERB	1	GRB	18	0.0	12.928	26.9	2.9E-5
3B 931204	2676	HERB	1	GRB	59	0.0	15.808	50.0	8.1E-5
3B 940206	2798	MER	13	SBPL	65	0.030	68.126	48.2	1.4E-4
3B 940210	2812	HERB	6	BPL	24	0.0	29.056	11.4	2.0E-5
3B 940217	2831	HERB	0	GRB	32	7.296	33.664	20.3	7.4E-5
3B 940228	2852	HERB	7	BPL	25	0.0	38.656	9.4	3.6E-5
3B 940301	2855	HERB	4	GRB	37	0.0	43.264	12.6	6.5E-5
3B 940302	2856	CONT	1	GRB	42	-3.072	152.576	23.0	2.2E-4
3B 940319	2889	HERB	4	GRB	10	0.064	63.488	5.8	3.6E-5
3B 940323	2891	MER	45	BPL	36	-2.048	24.350	18.6	4.3E-5
3B 940414	2929	HERB	4	GRB	36	0.0	46.208	9.9	4.6E-5
3B 940429	2953	HERB	3	GRB	33	0.0	25.088	26.7	2.7E-5
3B 940526B	2993	HERB	3	COMP	9	0.0	28.800	4.8	2.1E-5
3B 940526	2994	HERB	1	BPL	44	3.008	27.264	26.0	5.0E-5
3B 940529	3003	HERB	0	GRB	13	0.0	35.584	5.1	1.9E-5
3B 940619	3035	HERB	6	GRB	13	0.0	62.016	3.2	1.9E-5
3B 940623	3042	HERB	1	GRB	19	0.128	16.192	12.1	1.5E-5
3B 940703	3057	SHERB	5	BPL	22	27.456	92.800	47.0	2.3E-4
3B 940708	3067	HERB	6	GRB	25	0.0	7.744	35.2	3.0E-5
3B 940810	3115	HERB	3	GRB	21	10.944	30.656	18.3	1.8E-5
3B 940817	3128	HERB	5	GRB	43	20.416	48.000	20.8	6.1E-5
3B 940826	3138	HERB	6	GRB	18	7.808	17.408	25.1	1.1E-5
4B 940921	3178	HERB	2	GRB	22	0.033	24.768	35.0	5.4E-5
4B 941008	3227	HERB	5	GRB	14	82.176	93.056	8.7	1.2E-5
4B 941014	3241	HERB	6	GRB	37	18.560	44.736	18.3	3.0E-5
4B 941017	3245	MER	04	SBPL	182	4.894	86.558	23.4	1.6E-4
4B 941020 <sup>†</sup>	3253	SHERB	5	GRB	28	15.680	70.336	20.5	6.7E-5
4B 941023	3255	HERB	4	BPL	14	0.127	32.320	20.0	2.0E-5
4B 941121	3290	HERB	4	GRB	12	34.304	52.032	18.6	1.6E-5
4B 941228	3330	HERB	3	GRB	14	0.108	59.584	9.8	2.2E-5
4B 950104	3345	HERB	1	GRB	17	0.033	11.584	11.5	1.4E-5
4B 950111	3352	HERB	2	GRB	28	0.033	42.560	5.9	2.6E-5
4B 950208	3408	HERB	6	GRB	61	0.090	28.288	24.0	5.5E-5
4B 950211	3415	HERB	5	GRB	25	0.026	54.592	15.8	2.9E-5
4B 950301	3448	CONT	3	BPL	11	180.224	337.920	2.7	2.3E-5
4B 950305 <sup>†</sup>	3458	SHERB	4	GRB	17	0.033	23.040	11.1	2.1E-5
4B 950325	3481	HERB	2	GRB	21	37.184	47.616	55.7	2.7E-5
4B 950401	3489	HERB	5	GRB	15	0.116	18.624	9.6	2.6E-5
4B 950403	3491	HERB	3	GRB	52	1.792	17.344	61.2	4.4E-5
4B 950403B	3492	HERB	5	GRB	26	3.008	8.960	224.5	4.3E-5
4B 950425	3523	HERB	6	BPL	58	0.033	28.864	47.2	1.1E-4
4B 950513	3571	HERB	5	GRB	22	0.092	36.352	18.0	2.3E-5
4B 950522	3593	HERB	2	BPL	14	0.026	18.368	11.5	2.1E-5
4B 950701	3657	HERB	4	GRB	26	0.032	9.600	48.3	2.3E-5
4B 950701B	3658	HERB	5	GRB	30	0.026	11.392	19.5	2.0E-5
4B 950804	3734	HERB	4	GRB	15	0.147	3.712	55.0	2.0E-5
4B 950818	3765	HERB	1	GRB	31	51.584	73.280	41.7	3.4E-5
4B 950909	3788	CONT	3	GRB	23	0.0	67.584	8.3	3.9E-5
4B 951011	3860	HERB	5	GRB	16	0.033	29.760	6.4	2.9E-5
4B 951016	3870	HERB	5	GRB	16	0.026	5.440	30.5	1.2E-5

Table 1—Continued

Burst Name <sup>a</sup> (1)	Trigger Number (2)	Data Type (3)	Detector Number <sup>b</sup> (4)	Model Used <sup>c</sup> (5)	No. of Spectra (6)	Time Interval (s) Start (7)	Stop (7)	Peak Flux <sup>d</sup> (ph cm <sup>-2</sup> s <sup>-1</sup> ) (8)	Fluence <sup>d</sup> (erg cm <sup>-2</sup> ) (9)
4B 951102	3891	HERB	2	GRB	21	25.920	42.368	28.3	1.3E-5
4B 951203	3930	HERB	0	GRB	20	0.032	21.056	17.6	5.4E-5
4B 951219	4039	HERB	6	COMP	19	0.025	43.008	11.8	3.7E-5
4B 960114	4368	SHERB	0	BPL	25	14.784	27.200	142.2	1.2E-4
4B 960124 <sup>†</sup>	4556	HERB	5	GRB	23	0.026	4.992	28.8	1.6E-5
4B 960201 <sup>†</sup>	4701	HERB	1	GRB	21	7.232	26.304	10.3	2.1E-5
4B 960321	5299	SHERB	0	BPL	46	41.280	69.440	54.1	4.5E-5
4B 960322 <sup>†</sup>	5304	MER	57	GRB	59	0.024	26.904	23.5	7.3E-5
4B 960529	5477	HERB	1	COMP	20	0.091	10.048	76.6	3.5E-5
4B 960605	5486	MER	23	BPL	46	59.672	89.368	17.4	5.9E-5
4B 960607	5489	HERB	1	GRB	26	29.888	55.040	14.9	2.9E-5
4B 960623	5512	HERB	5	BPL	13	0.033	29.952	5.1	1.8E-5
4B 960807	5567	HERB	0	GRB	32	0.090	17.792	45.4	2.7E-5
4B 960808	5568	HERB	6	GRB	8	0.190	5.632	24.3	1.9E-5
5B 960831	5591	MER	67	BPL	49	-9.216	166.912	7.4	5.6E-5
5B 960924	5614	SHERB	6	BPL	27	7.360	13.120	490.0	1.5E-4
5B 961001 <sup>†</sup>	5621	HERB	2	GRB	25	0.026	10.304	51.2	2.9E-5
5B 961009	5629	HERB	6	BPL	35	0.033	15.936	9.5	2.1E-5
5B 961029 <sup>†</sup>	5649	MER	15	SBPL	351	1.941	123.285	55.6	1.8E-4
5B 961102	5654	MER	15	GRB	63	0.030	100.126	7.1	6.0E-5
5B 961202	5704	HERB	0	GRB	13	0.030	5.184	64.4	1.2E-5
5B 970111	5773	HERB	0	COMP	57	0.029	21.824	23.8	4.4E-5
5B 970201	5989	MER	015	GRB	41	0.024	1.688	279.4	1.0E-5
5B 970202 <sup>†</sup>	5995	HERB	1	BPL	60	0.090	21.632	24.4	7.3E-5
5B 970223	6100	HERB	6	BPL	35	0.090	18.368	35.3	4.2E-5
5B 970306	6115	HERB	2	BPL	15	0.150	107.776	3.3	4.0E-5
5B 970315	6124	SHERB	2	BPL	47	0.026	19.200	40.6	6.4E-5
5B 970411	6168	CONT	1	GRB	17	-12.288	102.400	18.3	8.2E-5
5B 970420	6198	HERB	4	GRB	45	0.045	11.968	145.0	6.4E-5
5B 970517	6235	HERB	5	GRB	9	0.090	7.232	31.7	1.5E-5
5B 970616	6274	HERB	1	BPL	20	42.240	127.040	21.3	3.9E-5
5B 970807	6329	HERB	4	GRB	31	0.045	47.744	12.6	3.9E-5
5B 970816	6336	HERB	7	SBPL	10	1.984	6.848	29.9	2.4E-5
5B 970828	6350	MER	57	COMP	113	0.030	96.030	15.3	7.4E-5
5B 970831	6353	HERB	0	GRB	32	0.033	123.008	5.1	5.0E-5
5B 970919	6389	MER	013	GRB	28	-14.016	24.601	12.2	3.4E-5
5B 970925	6397	HERB	7	GRB	19	0.092	35.584	10.4	2.4E-5
5B 970930	6404	HERB	6	GRB	20	0.058	11.648	42.0	2.1E-5
5B 971029	6453	HERB	1	BPL	45	0.033	117.312	7.0	5.8E-5
5B 971110	6472	CONT	1	SBPL	52	-2.304	276.224	23.0	1.7E-4
5B 971208	6526	CONT	6	SBPL	36	-5.120	199.680	3.5	9.4E-5
5B 980105	6560	HERB	7	SBPL	16	0.030	37.056	13.7	2.0E-5
5B 980124	6576	MER	046	SBPL	55	0.027	45.595	20.2	5.4E-5
5B 980125	6581	HERB	0	SBPL	17	42.688	64.768	85.0	2.9E-5
5B 980203	6587	MER	01	SBPL	94	0.030	36.126	57.0	1.3E-4
5B 980208 <sup>†</sup>	6593	HERB	3	SBPL	32	0.033	29.632	17.9	3.7E-5
5B 980225	6615	HERB	4	SBPL	16	85.120	164.096	3.2	5.7E-5
5B 980306	6629	HERB	1	GRB	12	180.608	254.144	12.9	4.5E-5
5B 980306B	6630	HERB	3	SBPL	17	0.042	20.992	21.9	2.2E-5
5B 980329 <sup>†</sup>	6665	HERB	0	SBPL	38	0.026	20.736	26.9	4.9E-5

Table 1—Continued

Burst Name <sup>a</sup>	Trigger Number	Data Type	Detector Number <sup>b</sup>	Model Used <sup>c</sup>	No. of Spectra	Time Interval (s)	Peak Flux <sup>d</sup>	Fluence <sup>d</sup>
(1)	(2)	(3)	(4)	(5)	(6)	(7)	(8)	(9)
5B 980703	6891	MER	13	SBPL	27	–34.816 59.550	4.8	3.7E–5
5B 980724	6944	HERB	6	SBPL	23	0.090 50.560	8.9	2.8E–5
5B 980803	6963	MER	26	SBPL	31	–2.048 24.607	30.9	4.4E–5
5B 980810	6985	HERB	3	SBPL	56	0.033 42.432	33.6	1.1E–4
5B 980821	7012	HERB	0	SBPL	32	0.091 30.784	38.0	3.9E–5
5B 980923	7113	MER	37	SBPL	133	0.024 38.424	167.3	4.5E–4

<sup>a</sup>Burst names are from Meegan et al. 1996 (3B Catalog) and Paciesas et al. 1999 (4B), and continue with a ‘5B’ prefix for bursts that occurred after the end of the 4B Catalog.

<sup>b</sup>Entries with multiple detectors indicate that summed data were used for the analysis.

<sup>c</sup>Model names are described in the text.

<sup>d</sup>Fluences are determined for the given spectral form and are integrated over the indicated time interval; peak fluxes have varying timescales. Thus, these differ from the 3B and 4B Catalog values.

†Overwriting event.

### 3.2. Selection of Appropriate Data Type

#### 3.2.1. Burst Data

There are several data types available for use, each of which has its own advantages and disadvantages. Table 2 shows the differences among all the BATSE data types available for burst studies, in terms of energy and temporal resolutions. The time coverage for the high energy resolution PHA data types (HERB/SHERB) varies, depending on the burst count rate, but is never longer than the burst data accumulation period (Table 3). Faced with the array of data products, several criteria have to be set to ensure the maximum scientific return from the analyses. In view of the fact that the LAD collecting area is almost 16× that of the SDs, data from the LADs are preferred. For continuum studies, the higher count rate, combined with the moderate energy resolution, is sufficient to determine spectral model fit parameters with good precision. The HERB data type has the highest energy resolution and sub-second time resolution (depending on the burst intensity), so it is the primary data type used for this effort. If the HERB accumulation finishes before the end of the burst, or if the HERB time resolution is not sufficient to resolve significant features in the time history, MER may be substituted. If that is not available, then CONT data can be used, especially in cases where the burst is longer than the burst accumulation time (Table 3) or the MER duration. The discriminator (4-channel) data are not used for this catalog since they lack sufficient energy resolution. Finally, there are occasions where an appropriate LAD data type is unavailable, such as loss of data transmission due to telemetry gaps. If the event is intense enough that the difference in collecting area does not matter much, the SD PHA data type SHERB may be substituted. It is also preferred in very intense events where the available HERB memory fills up before the end of the outburst. For the brightest of these, electronic effects such as pulse pile-up precludes analysis. In these cases (only two during the period covered by this catalog), the SD data are the only recourse for accurate spectral deconvolution. Table 1 gives the chosen data type in column 3, and the corresponding detector number(s) in column 4. In particular, note from the ‘SHERB’ entries in column 3 that SD data were used for only nine bursts out of the total sample.

The high energy resolution PHA data types HERB and SHERB are accumulated in a time-to-spill mode, not uniformly sampled in time. As originally configured, the flight software would end a spectral accumulation after 64k counts (or any other preset value) had been recorded in one of the LAD detectors. The detector picked to have its count accumulations monitored for this purpose is the one that was determined to have the highest count rate at the burst trigger time. Spectral data are only accumulated for the detectors that had the four highest count rates at the trigger time. The second ‘brightest’

Table 2. BATSE Burst Data Types

Data Type	Detector Type	# Energy Channels	# Spectra (# Events) <sup>a</sup>	Resolution (ms)	Detector Subset	Time Coverage
HERB	LAD	128	128	128 <sup>b</sup>	DSELH <sup>c</sup>	$\leq$ DISCSC
HER	LAD	128	—	( $\sim$ 300 s)	All	Background
MER	LAD	16	4096	16 & 64 <sup>d</sup>	DSELB <sup>e</sup>	163.84 s
CONT	LAD	16	—	2048	All	Continuous <sup>f</sup>
DISCSC	LAD	4	Varies <sup>g</sup>	64	DSELB <sup>e</sup>	Fixed <sup>g</sup>
PREB	LAD	4	32	64	All	–2.048 s
TTE	LAD	4	(32768)	0.128	DSELB <sup>h</sup>	Varies
DISCLA	LAD	4	—	1024	All	Continuous <sup>f</sup>
SHERB	SD	252	192	128 <sup>b</sup>	DSELH	$\leq$ DISCSC
SHER	SD	252	—	( $\sim$ 300 s)	All	Background
STTE	SD	256	(65536)	0.128	DSELB <sup>h</sup>	Varies
DISCSP	SD	4	192	2048, 128 <sup>b</sup>	All, DSELH	Continuous

<sup>a</sup>(S)TTE: Individual time-tagged events in parentheses.

<sup>b</sup>Minimum for time-to-spill, increases by 64 ms increments.

<sup>c</sup>DSELH: 4 detectors with ‘highest’ count rates, determined at trigger.

<sup>d</sup>The change to 64 ms resolution is after the first 32.768 s.

<sup>e</sup>DSELB: The 2–4 detectors with highest count rates, as determined at the time of the trigger (MER and DISCSC are summed over these detectors).

<sup>f</sup>Can serve as background data.

<sup>g</sup>Determined by the length of the data accumulation (see Table 3).

<sup>h</sup>Switches from the full set of detectors to the DSELB subset after approx. 30 ms.

Table 3. Burst Data Accumulation History

Date (TJD)	Seconds of Day <sup>†</sup>	# DISCSC Spectra	Accumulation Duration (s)
8362	0	3776	241.664
8366	0	2816	180.224
8367	5632	3776	241.664
8807	66200	2816	180.224
8810	78770	3776	241.664
8973	62418	8960	573.440
10091	6591	3776	241.664
10181	55298	8960	573.440
10464	71456	3776	241.664
10504	80943	8960	573.440
10983	71859	3776	241.664

<sup>†</sup>Date and time at which the accumulation mode went into effect.

detector records one spectrum for every two the brightest detector records, while the third and fourth brightest detectors record one spectrum for every two recorded in the second brightest. The minimum accumulation time is 128 ms; however, the incremental time resolution is 64 ms. A total of 128 spectra can be accumulated for the LADs, while 192 are available for SD spectra. After half of the LAD spectra have been accumulated, the on-board CPU tests the elapsed time against a commanded time parameter. If the actual time is larger, a multiplication constant (usually 2), which can also be changed from the ground, is then applied to the spectral accumulation parameter, until the memory fills or a preset time runs out (this is the ‘burst accumulation time’, which is also set from the ground – see Table 3). The time resolution of the two BATSE detector types is identical until the LADs fill up the on-board memory, at which time the electronics again determine whether it should change the accumulation criteria for the remaining SD memory. In a later change of the flight software, the total counts minus a ground-commanded fraction of the background counts, rather than the total counts alone, is compared with the fixed total counts accumulation criterion for each spectrum. To obtain approximately the same peak accumulations as before this change, the accumulation parameter is also lowered from the previous value of 64k counts to accommodate for the reduction of the total count rate by the background fraction. In this manner, periods where the burst activity has effectively returned to background levels are accumulated into one spectrum, while active portions of the burst are sampled nearly as rapidly as previously. The intention is to provide fine time-resolution spectra throughout a long event, without having to change to longer accumulations to cover the end.

### 3.2.2. Continuous and Background Data

Some cases exist where the selected burst in the catalog triggered the instrument during the data readout period (usually about 90 min) of a weaker event. In which case, data for the previous event not yet telemetered to the ground are overwritten in the BATSE memory by the new event; hence this class of events are called ‘overwrite’ triggers. During the burst data readout, the 64 ms trigger threshold is set to either the larger of the highest recorded 64 ms count rate in the brightest detector during the burst data accumulation period or the largest of the previous event’s three trigger thresholds. Given how the BATSE trigger operates, count rates in the *second* brightest detector must exceed the new 64 ms trigger threshold (the two other trigger timescales are disabled) before an overwrite event occurs. Thus, the overwriting event must be quite strong before it can trigger, and possibly some considerable portion of the emission may occur before the trigger. The PHA data do not have fine time resolution before the trigger, so an alternative data type (usually CONT)

must be chosen. Overwriting bursts are indicated with a dagger ( $\dagger$ ) in column 1 of Table 1.

The background rates are available in corresponding data types for each ‘class’ of energy resolution, as seen in Table 2. For example, the 128 channel HER data type is the appropriate background data for the HERB burst data type. Due to memory storage and telemetry limitations, the highest energy resolution background data are available in the lowest time resolution, typically  $\approx 300$  s for HER and SHER. The result of this is that only long-term variations of the background rate can be modelled in most cases. For background modelling, low-order ( $\leq 4$ ) polynomial behavior is assumed. Because the length of the background accumulations of HER and SHER data approach the timescale of background variations, the background model must predict the average background rate of an interval, rather than the background rate at the midpoint of the interval. As an example, consider the case that the background rate during three background accumulations is low, high, then low (Fig. 4). If we fit a second-order polynomial using points at the center of each accumulation, then the estimated rate for any time during the center interval will always be less than the true rate (Fig. 4–*dashed line*). The observed rates are averages over the accumulation intervals, so the background model should also be averaged over the intervals. The correct fit is obtained by minimizing the differences between the averages of the polynomial model and the observed rates (Fig. 4–*dotted line*). When they are available, we choose background spectra within  $\pm 1000$  s relative to the trigger, so that at least three spectra before and after the trigger can be used to provide a background model. For cases where the burst emission is over before the burst data memory has been filled, the post-burst portion may be used as part of the background. It is better to estimate the background as close as possible to the beginning and the end of the burst; however, care must be taken so as not to include a faint, fading portion of the burst. If less than six total background spectra are available, the order of the background model must be decreased from the default of four, so that the available degrees of freedom does not fall to zero or below. The model is fit separately to each energy channel, and the resulting  $\chi^2$  per degree of freedom examined for systematic problems. If any are found, the background selection is changed and re-fit until a suitable model is found.

### 3.3. Spectral Models Used

Due to the non-diagonal nature of the detector response function, the choice of spectral model to be used for fitting in some sense determines the outcome. Spectral deconvolution is never exact, since we are trying to guess an unknown function from a data set that has been passed through a filter that loses information. That is, we choose a candidate spectral

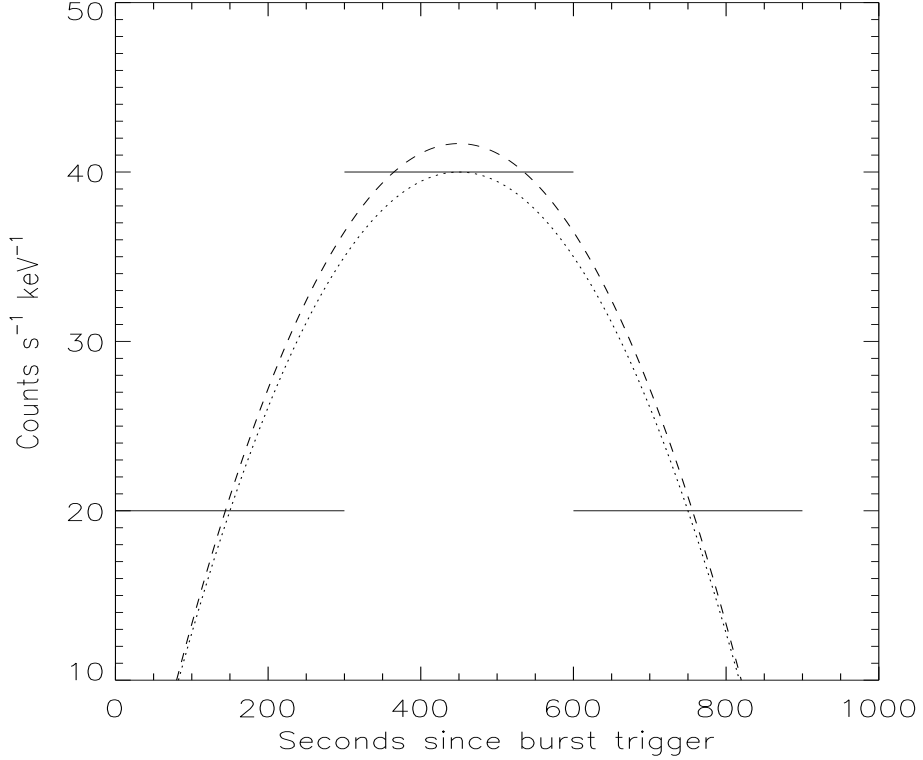


Fig. 4.— A simulated set of HER background histories, with a concave upwards behavior, showing two fits: one, a simple second-order polynomial in time using the average value for each rate fitted at the center, obviously underestimating the average rate (*dotted*), the other using integrated basis functions, where the average of the fitted model over the spectral accumulation time interval is the same as the data rate (*dashed*). In practice, a second-order fit to three background intervals would not be allowed.

form, with several parameters to be determined from the fit, and multiply it by the detector response function, which distributes photons at any given energy into counts data channels at all lower energies. The functional parameters are adjusted until a best fit is obtained. However, the best fit is only for the chosen model; there is no guarantee that a different model might not result in a better fit. Unfortunately, there is no best method to determine for each count spectrum the best possible functional form other than trying many different functions, optimizing each one over the available spectral parameters and choosing the one with the best  $\chi^2$ . In practice, we have drawn from a small set of ‘reasonable’ spectral forms, all empirically determined through experience. We do make the assumption, however, that a single spectral model suffices to fit every spectrum in a single burst, an assumption that can be tested using the  $\chi^2$  distribution. For each burst, the particular model used is given by a mnemonic (such as ‘GRB’) in column 5 of Table 1 that is explained in the following

discussion. The models and their parameters used in the preparation of this catalog are presented below as they appear in the data archive.

### 3.3.1. The GRB Model

The model typically chosen for spectral fitting of bursts is the empirical ‘GRB’ function (Band et al. 1993):

$$\begin{aligned}
 f_{\text{GRB}}(E) &= A(E/100)^\alpha \exp(-E(2+\alpha)/E_{\text{peak}}) \\
 \text{if } E &< (\alpha - \beta)E_{\text{peak}}/(2+\alpha) \equiv E_{\text{break}}, \\
 \text{and } f(E) &= A\{(\alpha - \beta)E_{\text{peak}}/[100(2+\alpha)]\}^{(\alpha-\beta)} \\
 &\quad \exp(\beta - \alpha)(E/100)^\beta \\
 \text{if } E &\geq (\alpha - \beta)E_{\text{peak}}/(2+\alpha),
 \end{aligned} \tag{1}$$

where the four model parameters are

1. the amplitude  $A$  in photons  $\text{s}^{-1} \text{ cm}^{-2} \text{ keV}^{-1}$ ,
2. a low-energy spectral index  $\alpha$ ,
3. a high-energy spectral index  $\beta$ ,
4. and a  $\nu\mathcal{F}_\nu$  ‘peak’ energy  $E_{\text{peak}}$ .

The parameter  $E_{\text{peak}}$  corresponds to the peak of the spectrum in  $\nu\mathcal{F}_\nu$  only if  $\beta$  is less than  $-2$ . Otherwise, the parameter value is identical to  $E_{\text{break}}$ , which marks the lower boundary in energy of the high-energy power-law component characterized by  $\beta$ . The ‘true’  $E_{\text{peak}}$  when  $\beta > -2$  lies at an unknown energy beyond the high end of the data, for 867 out of the 5253 spectra that had a well-defined value of  $\beta$  (16%). The ‘pivot’ energy of 100 keV serves as the energy at which the normalization of the function  $A$  is determined. Several words of caution are in order here: the GRB model parameter  $\alpha$  is an asymptote to the actual power-law slope realized by the data (Preece et al. 1998b). The inherent curvature of the model may or may not be well realized in the low-energy data, but there is no way the curvature can be adjusted arbitrarily by the spectral parameters. If all three parameters are well-determined, the curvature is fixed by the assumed functional form. There is another function that addresses this (see the SMPL model below), at the cost of an additional degree of freedom.

### 3.3.2. The COMP Model

If the GRB model break energy lies above the highest energy available to the detector so that  $\beta$  is ill-defined, or if  $|\beta|$  is so large that is essentially infinite (and thus numerically unstable), we must substitute a related form of the model with the high-energy power-law omitted:

$$f_{\text{COMP}}(E) = A(E/E_{\text{piv}})^\lambda \exp(-E(2 + \lambda)/E_{\text{peak}}) \quad (2)$$

where the four model parameters are

1. the amplitude  $A$ ,
2. the  $\nu F_\nu$  ‘peak’ energy  $E_{\text{peak}}$  in keV,
3. a low-energy spectral index  $\lambda$ ,
4.  $E_{\text{piv}}$  = a pivot energy in keV (always held fixed).

For historical reasons, the resulting model is called ‘COMP’, meaning Comptonized spectrum. However, the COMP functional form describes the physical thermal Compton spectrum only for the value  $\alpha = -1$ ; whereas, in fitting, there is usually no such restriction. Again, the pivot energy determines the energy at which the normalization  $A$  is calculated. For some soft spectra (not considered here), the value of the pivot greatly affects the numerical stability of the fit. If the peak energy is less than 10 KeV, for example, the normalization determined at 100 keV would be quite large and may cause a numerical overflow; in which case, the pivot should be changed to 10 keV. In the catalog, this and the corresponding parameters in the models below are always held constant throughout the series of fits in each burst at 100 keV.

### 3.3.3. The BPL Model

In cases where a sharp curvature of the spectrum results in an unacceptable value of  $\chi^2$  for a fit to the intrinsically smooth GRB spectral form, a broken power-law (‘BPL’) model often generates better results:

$$f_{\text{BPL}}(E) = A \begin{cases} (E/E_{\text{piv}})^{\lambda_l} & \text{if } E \leq E_b \\ (E_b/E_{\text{piv}})^{\lambda_l} (E/E_b)^{\lambda_h} & \text{if } E > E_b \end{cases}, \quad (3)$$

where

1.  $A$  = amplitude in photons  $\text{s}^{-1} \text{ cm}^{-2} \text{ keV}^{-1}$ ,
2.  $E_{\text{piv}}$  = pivot energy in keV (always held fixed),
3.  $\lambda_l$  = index below break,
4.  $E_b$  = break energy in keV,
5.  $\lambda_h$  = index above break.

No known physical model corresponds to this spectral function. However, a sharp feature in the fitted data could be a result of an absorption edge arising in the source. Given the likelihood of large Lorentz motions of the emitting material, a scenario where a sharp spectral feature could survive intact enough to be observable is difficult to arrange. The ambiguity of spectral deconvolution makes it likely that the unknown source spectrum may be less sharp than the model, while not allowing enough smooth curvature of the kind that characterizes the GRB function.

#### 3.3.4. The SBPL Model

Finally, there is an intermediate model where the sharp spectral break of the BPL model is replaced by a smooth join of the two power law components, hence the name: smoothly-broken power law ('SBPL'). This model has the additional freedom to specify the width of the region of curvature (see also: Ryde & Svensson 1998):

$$\begin{aligned}
 f_{\text{SBPL}}(E) &= A(E/E_{\text{piv}})^b 10^{(\beta - \beta_{\text{piv}})} , & (4) \\
 \beta &= m\Delta \ln \left( \frac{e^\alpha + e^{-\alpha}}{2} \right) & \beta_{\text{piv}} &= m\Delta \ln \left( \frac{e^{\alpha_{\text{piv}}} + e^{-\alpha_{\text{piv}}}}{2} \right) \\
 \alpha &= \frac{\log_{10}(E/E_b)}{\Delta} & \alpha_{\text{piv}} &= \frac{\log_{10}(E_{\text{piv}}/E_b)}{\Delta} \\
 m &= \frac{\lambda_2 - \lambda_1}{2} & b &= \frac{\lambda_1 + \lambda_2}{2}
 \end{aligned}$$

where

1.  $A$  = amplitude in photons  $\text{s}^{-1} \text{ cm}^{-2} \text{ keV}^{-1}$ ,
2.  $E_{\text{piv}}$  = pivot energy in keV (always held fixed),
3.  $\lambda_1$  = lower power-law index,

4.  $E_b$  = break energy in keV,
5.  $\Delta$  = break scale in decades of energy,
6.  $\lambda_2$  = upper power-law index.

This model is derived as follows: we want  $d(\log f)/d(\log E) = y$  (the power-law index as a function of energy) to be a linear function ( $y = mx + b$ ) of the hyperbolic tangent  $x = \tanh\left[\frac{\log_{10}(E/E_b)}{\Delta}\right]$ , which interpolates smoothly between  $-1$  and  $1$ . This makes the log slope a horizontal line at  $y = \lambda_1$  for small  $E$ , smoothly changing to a horizontal line at  $y = \lambda_2$  for large  $E$ . For this model, the break scale parameter  $\Delta$  is fit to its best value for the sum of all the spectra in the burst. For the subsequent fits to individual spectra,  $\Delta$  is held fixed at the best-fit value, rather than being allowed to be freely determined. The reason for this is that  $\Delta$  can not be determined better than the instrumental energy resolution, so the additional free parameter interferes with the others resulting in considerable cross-correlation that manifests itself in large errors. This is especially true for the individual spectral fits, where the statistics are worse than that of the total spectrum of the burst. Since  $\Delta$  is held fixed throughout the series of spectral fits, the result is a model function with the same number of parameters of interest as the GRB function, but with a controllable curvature.

### 3.3.5. Spectral Model Selection

In the nominal BATSE energy band, GRBs can be successfully fit with one or more of these models; four parameters or fewer are sufficient. As can be seen from Table 1, column 5, the GRB model is used most frequently, for 95 out of the total 156 bursts. This is followed by BPL (32 times), SBPL (23) and COMP (6). The actual choice of model was somewhat qualitative: if the GRB model did not result in a reduced  $\chi^2$  distribution for all spectra fitted within a burst that was approximately centered on one, the BPL model was tried. If there was some indication from the  $\chi^2_\nu$  distribution that the BPL model was inadequate, then the SBPL was used. The COMP model is used for those cases where the high-energy power law fit failed in more than  $\sim 30\%$  of the individual spectra, resulting in either exponential overflow errors or an indeterminate value for  $\beta$ .

Regardless of the model chosen, the region of applicability for the model does not extend beyond the energy interval fitted (see Figure 5). In fact, there are good reasons not to trust an extrapolation of these spectral models to low energies. First, at some energy around 1 keV, interstellar absorption from Galactic material must introduce a cut-off in

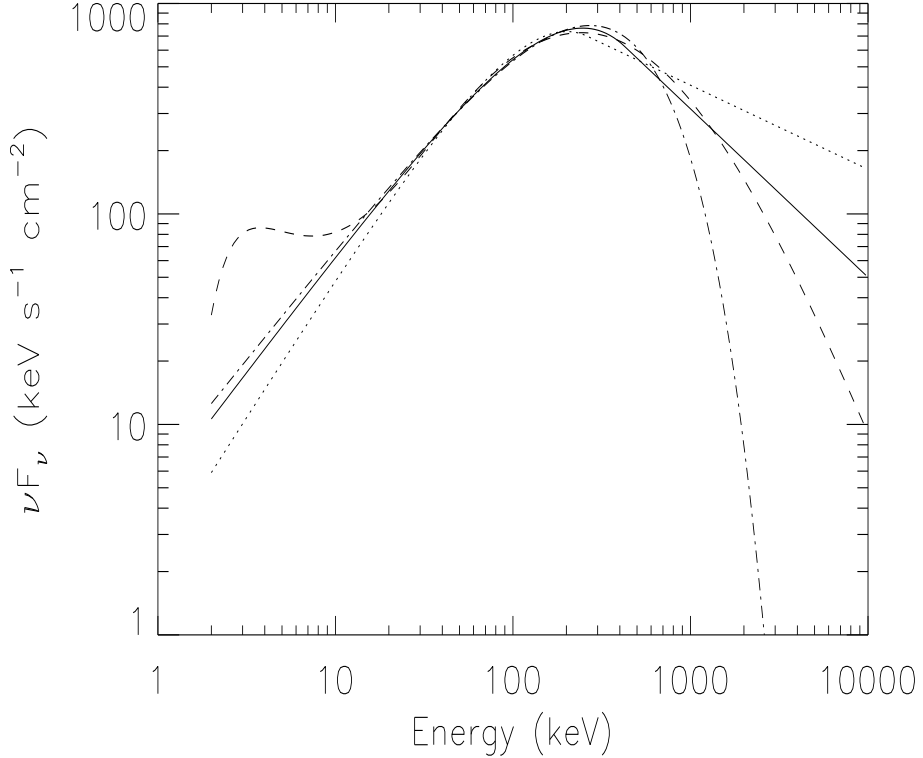


Fig. 5.— Several models that acceptably fit BATSE data from SD #5 for the first peak of 3B 940210, 15.68–33.28 s. The models (GRB: *solid*, GRB with  $\alpha$  fixed at  $-2/3$ : *dotted*, Compton Attenuation Model [Brainerd (1994)]: *dashed* and COMP: *dot dashed*) are very similar in the energy range for which the BATSE data has good S/N, 20 to  $\sim 1000$  keV, but diverge greatly below and above that range.

the observed counts spectrum, if it could be measured. At slightly higher energies, but still below the LAD energy threshold, a considerable fraction (15%) of all burst spectra have a measured excess in the 7–20 keV band (Preece et al. 1996). This is corroborated by the *Ginga* observations of GRB spectra to energies as low as 2 keV (Strohmayer et al. 1998). In some of these low-energy spectra, there is also evidence of a low-energy spectral break distribution, complementing the well-known  $E_{\text{peak}}$  distribution (Mallozzi et al. 1998). At higher energies, the picture is not as clear. Certainly, when it could be observed, the high energy power-law is seen to continue up to very high energies in the SMM, COMPTEL, EGRET, and BATSE SD data (Matz et al. 1985, Hanlon et al. 1995, Kippen et al. 1995, Dingus 1995, Briggs et al. 1999b). However, a  $-2$  power law (consistent with what has been observed) can not be extended upwards in energy indefinitely, as it represents the emission of equal power per unit energy interval; there must be an energy (currently unobserved) at which the spectrum is attenuated. For most bursts, with high-energy

power-law spectral indices  $< -2$ , this is not an issue. However, there is still the question: Where, exactly, do the observed non-thermal power law spectra end in energy? Eventually, broad-band spectroscopy may deliver an answer, but for now, it is unjustified to extend the fitted model spectra beyond the energies that were used in the fit.

#### 4. The Spectral Catalog

We have performed spectral fitting on 156 bright bursts observed with BATSE. The method we use in each case starts with a preliminary spectral fit to the sum of all selected spectra in a burst using the GRB model. The resulting value of  $\chi^2$  and the pattern of residuals from the model indicate whether another spectral model from our set should be tried, as described in the previous section. When the best model and parameter set for the summed spectra has been found, these become the starting point for a series of fits to each of the spectra in the burst. The average spectral parameters provide a reasonable set to fall back to in case one or more of the individual parameters is undetermined from the data. We then compare the reduced  $\chi^2$  distribution with unity as a final check on the selected model. In some extreme cases, where one of the spectral parameters is undetermined in a large fraction of the spectra (usually the high-energy power-law component), a different model is tried. In the end, we have a series of spectral parameters as a function of time.

The results are archived as a series of `ascii` files that are available electronically<sup>1</sup> having a consistent format that allows the whole series to be read by a standard procedure. A simple reader accompanies the archive, although the files can be parsed easily using any computer programming language. For the description of the catalog file format below, we will use as an example the file, `HH_1085_4.BAT`. Each file's name follows a standard convention: first, the data types used in the analysis for the particular event are encoded at the head of the name. ‘HH’ in the example represents HERB / HER, that is: HERB for the burst data, HER for the background; ‘MC’ is for MER / CONT, ‘SS’ for SHERB / SHER, while ‘CO’ stands for CONT data only. The name contains the BATSE trigger number (see Table 1) as this is a concise unique identifier (‘1085’ in the example file), whereas the burst name, ‘3B 911118’ would be ambiguous for dates with more than one burst observed in the day. In Table 1, we have added a letter that indicates the relative brightnesses of the several events that fall on one day (for instance, 3B 910814C [# 676] and 3B 910814 [#678]). Finally, the number corresponding to the detector that was selected for

---

<sup>1</sup>On the World Wide Web: <http://www.journals.uchicago.edu/ApJ/journal/> (this address may change when the data are actually published – there is nothing available yet)

the analysis is included ('4'), except for the MER files, where several detectors are summed and the detectors are omitted. The name always ends with the extension '.bat'.

#### 4.1. Header Data

We will reproduce portions of the example file's content below, exactly as it appears in the electronic archive, and describe each element in the general case. Each data file can be roughly divided into a standard header section and the fit data section. The general event information portion of the example file's header follows:

Current lookup parameters:

```
Burst number: 1085
Start day: 8578 Start sec: 68258.023
Data types: HER HERB
Detectors: 4
```

Observed selection start and stop times:

```
OBS_START: 0.000000 OBS_STOP: 13.6960 51 Spectra
Time Range: (-7.00000, 21.0000) seconds
Rate Range: (2.00000, 40.0000) counts/s-keV
```

Selected Energy bins lower and upper thresholds (keV):

```
LOWER_THRESH: 28.4235 UPPER_THRESH: 1862.51 115 Bins
Energy Range: (10.0000, 2000.00) keV
Rate Range: (0.000000, 308.096) counts/s-keV
```

Background selection start and stop times:

```
BACK_START: -1661.53 BACK_END: -449.112 2 Spectra
BACK_START: 28.8640 BACK_END: 914.856 2 Spectra
```

Order of the background model: 2

The first block contains information concerning the event itself, starting with the BATSE trigger number: 'Burst number: 1085'. This can be used in reference to column 2 of Table 1 to find the BATSE catalog name for the event in column 1: '3B 911118'. The date is given in TJD: 'Start day: 8578', that is: Julian Day minus 2,440,000.5, and the time of the event trigger in seconds of day (UT): 'Start sec: 68258.023'. Following this, there is information about the data selection; first, the data types used, 'Data types: HER HERB'

and the selected detector number(s): ‘**Detectors:** 4’. Note that in this example ‘4’ means detector #4 was selected, *not* that four detectors’ data were used. The data selection also gives an indication of the BATSE detector type, in that all data types for the SDs start with the letter ‘S’ (with the one exception being ‘DISCSP’, which is not used in this catalog; see Table 2). Here, the HERB data is generated by LAD #4, with HER for the background data. The next few blocks are concerned with the data selection ranges; first, the start and stop times with respect to the BATSE trigger time and the number of selected unbinned spectra: ‘**OBS\_START:** 0.000000 **OBS\_STOP:** 13.6960 **51 Spectra**’. Next, the energy selection interval is given, with the corresponding number of data bins: ‘**LOWER\_THRESH:** 28.4235 **UPPER\_THRESH:** 1862.51 **108 Bins**’. Finally, details of the background selection are presented as groups of selected spectra; the two statements ‘**BACK\_START:** -1661.53 **BACK\_END:** -449.112 **2 Spectra**’ and ‘**BACK\_START:** 28.8640 **BACK\_END:** 914.856 **2 Spectra**’ show that the background model consists of four spectra in two groups, one before and one after the burst interval (0. – 13.69 s); the polynomial order of the background fit is 2, as seen in the line: ‘**Order of the background model:** 2’. The ‘**Time Range:**’, ‘**Rate Range:**’ and ‘**Energy Range:**’ values define view windows centered on the selected time history and integrated spectrum and were generated as part of the data preparation step in the analysis procedure; as such, they have little bearing on the catalog. Taken together, all these values could be used to restore the data selection and views to the ones used in the preparation of this catalog.

The next group of information details the model used, and the names of the parameters.

11 columns are labeled:

Broken Power Law: Amplitude (p/s-cm<sup>2</sup>-keV)  
Broken Power Law: Pivot E =fix (keV)  
Broken Power Law: Index < BE  
Broken Power Law: Break E (keV)  
Broken Power Law: Index > BE  
Broken Power Law: Photon Flux (ph/s-cm<sup>2</sup>)  
Broken Power Law: Photon Fluence (ph/cm<sup>2</sup>)  
Broken Power Law: Energy Flux (erg/s-cm<sup>2</sup>)  
Broken Power Law: Energy Fluence (erg/cm<sup>2</sup>)  
Broken Power Law: Reduced Chi-squares  
Reduced Chi-squares (Chi-squares in Uncertainties): 111 Degrees of Freedom  
Burst Time History (Counts/s-keV)

In this example, these are the labels of the 11 columns of the fit parameters (and their uncertainties, which follow) plus an additional row containing the number of degrees of freedom for the fit. In each label but the last, the formal model name: ‘**Broken Power Law:**’ comes before the parameter name: ‘**Amplitude (p/s-cm<sup>2</sup>-keV)**’. The BPL model has five parameters, as discussed above, these make up the first five labels. Each parameter that has been fixed to a constant for the duration of the fit is indicated with ‘**=fix**’, as in the label ‘**Broken Power Law: Pivot E =fix (keV)**’. For each model, the columns that follow the fit parameters contain instantaneous flux and accumulated fluence: ‘**Photon Flux (ph/s-cm<sup>2</sup>)**’ and ‘**Photon Fluence (ph/cm<sup>2</sup>)**’. These have been numerically integrated over the selected energy range. In addition, corresponding energy fluxes and fluences have been calculated by including a factor for the energy in the integral: ‘**Energy Flux (erg/s-cm<sup>2</sup>)**’ and ‘**Energy Fluence (erg/cm<sup>2</sup>)**’. The peak flux in photons s<sup>-1</sup> cm<sup>-2</sup> can be found in the row containing the maximum value for the ‘**Photon Flux**’ column. The timescale for this calculation of peak flux is, by necessity, the accumulation time (or time bin width) for the spectrum corresponding to the row containing the peak value. The total fluence is contained in the final row of the ‘**Energy Fluence**’ column, as this parameter records the fluence integrated up to including that time. Either fluence parameter can stand as a proxy to the time since the beginning of the burst in demonstrating relationships between fluence and the other fit parameters, as was done for  $E_{\text{peak}}$  in GRB peak emission (Liang & Kargatis 1996, Crider et al. 1997). Since the time selections and timescales may differ from those in the official BATSE catalogs, these values for peak flux and fluence will almost certainly not exactly match the corresponding catalog values; however, they incorporate the spectral evolution throughout the burst, at the best available spectral resolution. The last two rows of data always contain the reduced  $\chi^2$  values for each fit, ‘**Broken Power Law: Reduced Chi-squares**’, and the actual count history (integrated over the selected energy bins), with the label: ‘**Burst Time History (Counts/s-keV)**’. In addition, we indicate the number of degrees of freedom for each spectral fit (111 in this case, which is constant throughout the burst) in a comment line that appears in the same relative position between the corresponding labels for reduced chi square and burst time history in each of the catalog data files: ‘**Reduced Chi-squares (Chi-squares in Uncertainties): 111 Degrees of Freedom**’. The actual  $\chi^2$  values can be found in the column that would ordinarily correspond to the uncertainty of the ‘**Reduced Chi-squares**’ column.

Next, the selected start and stop times for the spectral accumulations are given, in seconds relative to the burst trigger time:

```
50 time bins processed; start and stop times:  
0.000000    0.896000
```

0.896000	1.21600
1.21600	1.47200
1.47200	...

These time bins correspond to the rows in the data arrays; the number of rows is given first: ‘50 time bins’, representing the number of *binned* spectra; thus, this number can be different from the number of unbinned spectra in the ‘OBS\_START: 0.000000 OBS\_STOP: 13.6960 51 Spectra’ header line. Here, two spectra have been combined into one to satisfy the minimum S/N requirement, reducing the number of time bins processed by one to 50. Usually, the start time of one time bin will match the stop time of the previous bin; however, in the case of gaps in the data, or in case quiescent periods of the burst were skipped, these will not be the same.

#### 4.2. Fit Parameters and Uncertainties

There are two arrays of data; one each for the parameter values and their uncertainties. Their dimensions are listed first:

Batch Fit Parameters:	11	X	50		
0.0146409	100.000	-0.269407	326.031	-2.19617	6.27032
5.07425	3.31890e-06	2.68582e-06	0.765253	6.70804	
0.0349295	100.000	-0.288559	284.916	-2.39224	12.6129
8.51135	5.53011e-06	4.19282e-06	1.10751	11.3185	
0.0459018	100.000	-0.277344	280.340	-2.44527	16.5090
11.9836	7.19965e-06	5.70708e-06	0.940453	14.0348	
0.0592305	100.000	-0.285810	247.583	-2.43234	18.5416
14.8440	6.65124e-06	6.73318e-06	1.27628	16.1302	
0.0757569	100.000	-0.305579	201.955	-2.13975	22.2641
...					

In this case, there are eleven columns that correspond to the eleven column labels discussed above. There are 50 rows of data, corresponding to the 50 time bins of accumulated spectra. In this representation, each row has been split into two, to accommodate the eleven columns of data. A single column of this table represents the time history of the corresponding fit parameter (or other value, as indicated above) over the time history of the burst. For comparison, the count rate history, summed over the selected energy bins, is found in the last column. Notice that the column corresponding to the parameter

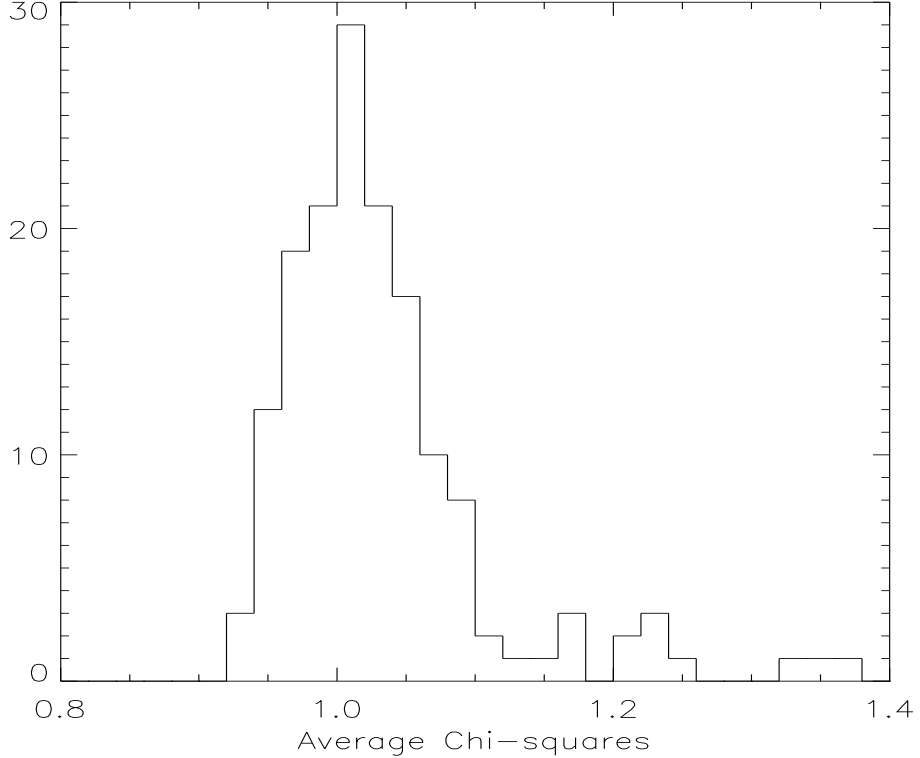


Fig. 6.— Total reduced  $\chi^2$  distribution for the sample of 156 bursts.

that was fixed ('Broken Power Law: Pivot E =fix (keV)') has all identical rows, as appropriate for a parameter held constant throughout. Also, the seventh and ninth columns are monotonically increasing, as these correspond to the accumulated fluences. When the reduced  $\chi^2$  values (in the tenth column) are displayed as a histogram they should be distributed fairly uniformly around 1.0 for an acceptable series of fits. Any deviation of the centroid of the distribution from 1.0 by more than  $3\sigma$  (as defined by the HWHM of the distribution) indicates possible systematic effects. Figure 6 shows the histogram of centroids for the individual reduced  $\chi^2$  distributions for the entire catalog. Some bursts are so intense in individual spectra that they belong to the regime where the systematics inherent in our model of the detector electronics and response dominate over the counts statistics, and so these have unusually high  $\chi^2$  values.

The final block of data lists the uncertainties for each of the fitted parameters (except that  $\chi^2$  is given in the place of an uncertainty for the reduced  $\chi^2$ , as discussed above). The uncertainties are given as the  $1\sigma$  errors derived from the covariance matrix of the fit. The given error estimate assumes the derived uncertainty is symmetrical about the best fit value of the parameter, which is good to first order, where each parameter is considered singly. To

know the error distribution in more detail requires creating a map of how  $\chi^2$  changes near the fitted parameter value. As the result depends upon the number of total parameters that are of interest for the particular question being asked, such analyses are not appropriate for a general-use catalog. Note that the fitting process may not have been able to determine the value of some parameters from the data. Such cases are flagged as indeterminate with a zero in the uncertainty. The fitting routine automatically fixes the value of an indeterminate parameter to the best-fit value determined for the integrated spectrum, while it attempts to optimize the fit for the remaining parameters for that particular spectrum. The parameter is allowed to vary again as usual when the next spectrum in the time series is fit.

In some cases, there may be correlations between parameters that are not evident from their individual distributions over each event. These may be recovered by observing a correlation in the scatter plot of the two parameters. Some of these correlations may arise from physical processes associated with GRB emission while some may be related to the statistics of parameter estimation when the two parameters are considered jointly for the chosen model. In the latter case, a more detailed analysis of the parameter uncertainties will have to be made. This was done, for example, for the low-energy power-law spectral index  $\alpha$ , obtained by either the GRB or the BPL model, to make a direct comparison with a specific prediction associated with a particular model (Preece et al. 1998b). Simulations of the error distribution for different values of  $\alpha$  indicated that larger (less negative) values had systematically larger errors associated with them, as was indeed observed.

## 5. Results

### 5.1. Distributions of Spectral Parameters

To get a general idea of the contents of the catalog, we present here the overall distributions of the three spectral parameters that have equivalents in each of the spectral models we have used for fitting (see Figures 7, 8 & 9). Each distribution is made up of the fitted parameters from 5500 different spectra, except for the high-energy power-law index distribution, which has 5253, since  $\beta$  sometimes was omitted from the fits. This occurred either because the parameter was absent from the model fitted (as in the COMP model) or because it was ill-determined and so it is fixed in value as discussed above. This will happen for spectra where there are not enough high-energy counts to constrain the value.

The low-energy power-law index  $\alpha$  distribution is seen not to overlap significantly with that of the high-energy ( $\beta$ ; see Figures 7 & 9). Even though the distribution of  $\alpha$  falls sharply on the high end toward +1, the edge is not as sharp as the expected statistical

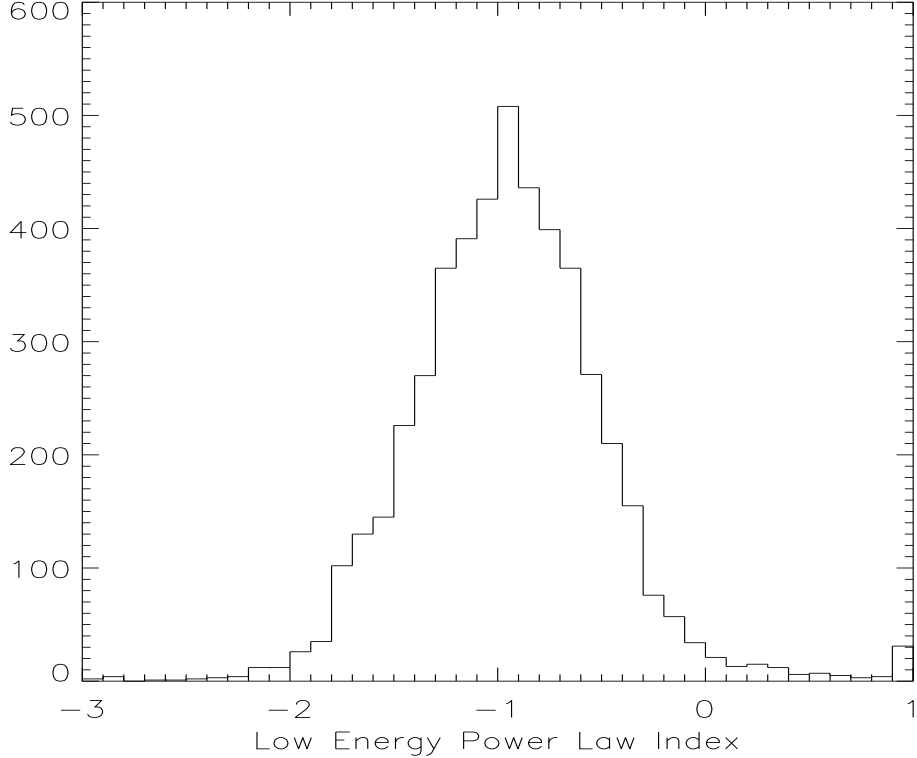


Fig. 7.— Low-energy power law index distribution for the entire sample.

error, assuming that all bursts have that same value of  $-1$  (or even  $-2/3$ , as expected from single-particle synchrotron emission – Preece et al. 1998b). That being said, it is interesting that the most likely value for  $\alpha$  is  $-1$ , not  $-2/3$ , so this number should arise naturally out of the physics of the emission mechanism. So far, an explanation that requires this value has not surfaced. However, the spread in values is also significant, especially those that are greater than  $-2/3$ , indicating bursts where synchrotron emission alone is not an option.

Spectral evolution within many of the bursts analyzed here has two consequences: First, the dataset consists of series of parameters, some of which appear to be correlated from one spectrum to the next, so the total distributions presented here consist of points that may not seem to be statistically independent. However, spectral evolution within a burst is defined by the observation that some spectral shape parameter is changing over the history of the burst, implying there is an intrinsic spread to the distribution related to the evolution of the parameter. That being said, it is still remarkable that the spectral break parameter, which has been the single most important signifier for spectral evolution (Ford et al. 1995), has a distribution (Figure 8) with a half-maximum full width less than a decade in energy. The significance of this is all the more emphasized by the fact

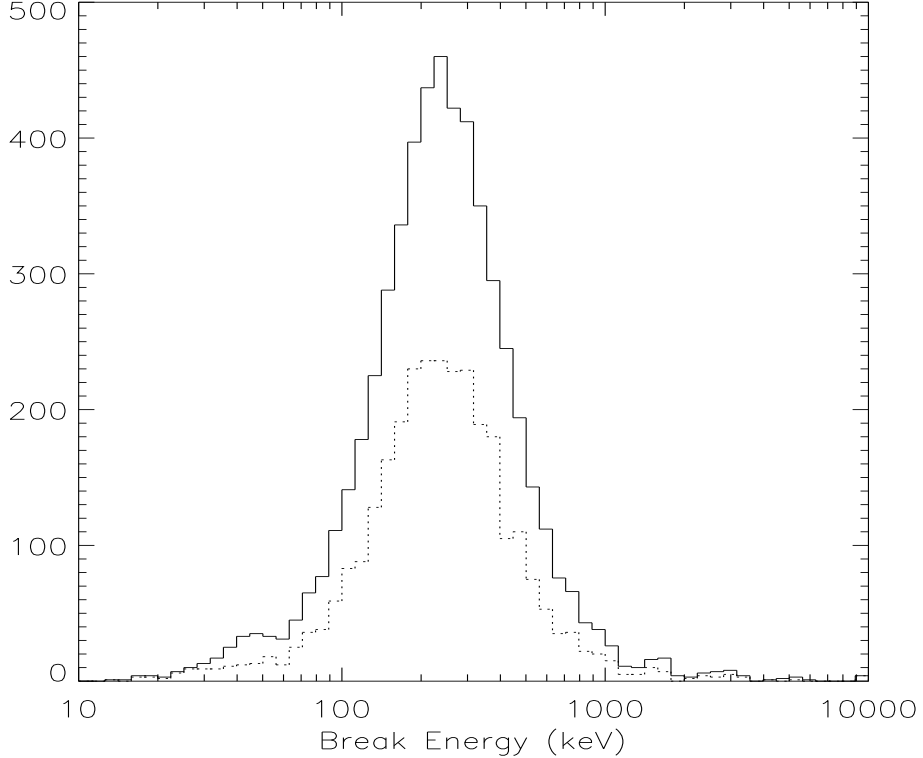


Fig. 8.— Break energy distribution for the entire sample (*solid line*). The subset of bursts *not* fit with the GRB model is also shown (*dotted line*).

that, out of all three spectral shape parameters, the break energy is the only one that is sensitive to relativistic motion between the source and the detector. On the one hand, cosmological red-shifting of GRB sources has been inferred from the shifts between break energy distributions for different peak flux bands (Mallozzi et al. 1995). In the present work, most of the bursts selected could be considered to belong to a single intensity group, so this effect should not be present (see Figure 3). However, given that bursts are now known to have considerable spreads in their intrinsic luminosities, it is highly likely that the bursts making up the sample set come from a large variety of distances, with an associated spread in red-shifts. This is clearly not evident in the observed distribution; the spread from  $z$  could easily be a factor of a few, but that would imply a correspondingly narrower intrinsic distribution. On the other hand, the presence of very high energy photons in many bursts implies very high Lorentz boosting of the emitting regions (Matz et al. 1985, Hurley et al. 1994) in the blast wave scenario (Goodman 1986, Mészáros & Rees 1993, Rees & Mészáros 1994). It has been noted by Brainerd (1994) that, despite a sensitive dependence upon the Lorentz boost factor, the break energy distribution does not seem to fill the pass band of the detectors, rather it is confined mainly to within a single decade of energy, as

seen clearly in Figure 8. Detailed modeling of the threshold detection efficiency for bursts with high and low break energies (Brainerd 1999), as well as an extensive search yielding negative results for a class of ‘high break energy’ bursts undetectable by BATSE in the SMM data (Harris & Share 1998), together indicate the importance of the narrowness of the distribution as a clue to the source emission mechanism.

## 5.2. General Discussion

There appears to be a second population of low-energy spectral break bursts, as evidenced by the second, smaller peak in Figure 8 centered at  $\sim 45$  keV. Although the energy is not coincident with the lowest energy available to be fitted, it may be that the grouping of low-energy breaks near the lowest available energy represents a ‘pinning’ of the parameter at a low value, whereas the spectrum actually does not significantly change slope below that value. The GRB model has a large intrinsic curvature below the break energy that is related to how the spectrum smoothly joins to a low-energy power-law component. Depending on the difference  $\alpha - \beta$ , which is typically close to 1, this fixed-curvature portion of the function can span several tens of keV above the lowest available energy. This can be tested by examining the distribution that results when the fitted values derived from the GRB model have been removed from the data set. In this case, most of the second peak vanishes, as seen in the dotted histogram in Figure 8. There is still the open question of the reality of a second, low-energy, continuum spectral break in some GRBs, since there is tantalizing evidence for this from the *Ginga* data set (Strohmayer et al. 1998). Most of the bursts in the *Ginga* sample have fitted  $E_{\text{break}}$  values that cluster around the peak of the BATSE distribution (Figure 8), however, 6 out of the 22 total have values below 10 keV. BATSE SD discriminator data has the potential to resolve some of this issue by extending spectral fits to BATSE data to lower energies (although not below 8 keV), indicating that four out of 86 bursts fall into the category of low-energy spectral breaks (Preece et al. 1996).

The general results from previous work on GRB spectroscopy are confirmed and expanded in the current database. A spectral form with two power law segments connected by some curvature seems to be the most prevalent acceptable model (Band et al. 1993). However, the COMP model, with no high-energy power law portion, was found to be an acceptable fit to all spectra in a single burst for six bursts out of the total sample. This may reflect the broad classification of bursts into high-energy (HE) and no-high energy (NHE) (Pendleton et al. 1997). There, as here, the phenomenon is characterized by a somewhat arbitrary division of a smooth distribution of high-energy behaviors into two

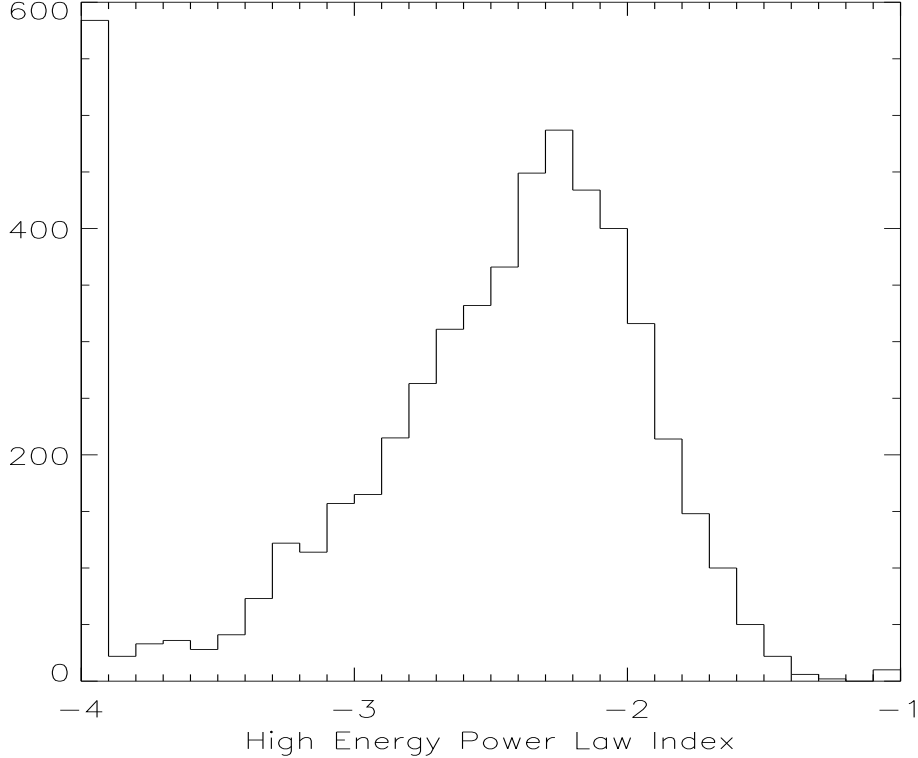


Fig. 9.— High-energy power law index distribution for the entire sample. All spectra that either do not have  $\beta$  values or that have values  $< -4$  have been included in the lowest bin.

groups. Here, we used the COMP model for those cases where the high-energy power-law index was poorly constrained in an initial global fit to the sum of all selected spectra within a burst. We took a value of the high-energy power-law index of  $< -4$  to indicate a poor constraint, since in practice many of the spectra fitted individually in such a case resulted in a poorly-determined value, or worse, a math underflow error in the function evaluation. Despite this index cut for the global spectrum in each burst, many individual spectral fits result in very large negative values for the index, which have been added to the lowest bin in Figure 9. Altogether there are 308 spectra with high-energy power-law indices below  $-4$ , in addition to the 247 spectra from the six bursts fit with the COMP model, or 10% of the spectra fitted that effectively do not have a high-energy power-law component. This is also in accordance with the results that NHE portions exist within HE bursts (Pendleton et al. 1997). There are differences, in that here, we do not take into account the effect of the break energy on whether a burst has high-energy emission, since, if the break energy is sufficiently high, the high-energy portion of the burst may not be well determined.

### 5.3. Concluding Remarks

It is our hope that this data set will continue to be useful for correlative analyses and testing of theoretical predictions. It has already generated some results of this nature, based on preliminary versions of the catalog. The peak of the high-energy power-law distribution is the same as reported before,  $-2.25$  (Preece et al. 1998a), although now with much better statistics. This is expected, as the data set used previously is a subset of the current one. In the previous work, the distribution for the average of the high-energy power-law index over each burst was presented, while here, we have shown the entire time-resolved distribution. Crider et al. (1997) have looked into bursts with unusually high values for the low-energy power-law index, as a possible indicator for saturated synchrotron self-Compton in isolated peaks of emission. The overall distribution of low-energy power-law indices has lead to a challenge to the validity of the synchrotron shock model (Katz 1994a, Tavani 1995). Indeed, the distribution of  $\alpha$  is centered on  $-1$ , which should be accounted for by any valid model. It is also too wide to accommodate the strict limit of  $-2/3$  that is imposed by the synchrotron shock model. The narrowness of the energy break distribution is also important. Many other studies can be constructed that correlate parameters within individual bursts, for example, or study average behavior over the entire population.

Following the present work, there will be two additional spectroscopy catalogs, one with fits to the peak flux and integrated fluence spectra using medium energy resolution BATSE data (Mallozzi et al. 1999), and the other presenting direct deconvolved spectra using four-channel discriminator data for throughout each burst (Pendleton et al. 1999). These catalogs will be concerned with the spectroscopy for larger burst samples than we have been able to analyze here, given our requirements. The medium energy resolution data can provide spectral parameters similar to those presented in the current work for the peak flux and total fluence spectra for most bursts in the BATSE catalog. For very weak bursts at the detector threshold, data with very coarse energy resolution may be employed to determine spectral hardness parameter evolution for every event.

Thanks to the BATSE operations team for some timely peak flux and fluence calculations, especially Surasak Phengchamnan, Burl Peterson and Maitrayee Sahi.

## REFERENCES

Band, D. L., et al. 1992, *Exp. Astron.*, 2, 307

Band, D. L., et al. 1993, *ApJ*, 413, 281

Brainerd, J. J. 1994, *ApJ*, 428, 21

Brainerd, J. J. 1999, *ApJ*, in preparation

Briggs, M.S. 1995, in “Gamma-Ray Bursts, 3rd Huntsville Symposium”, ed. C. Kouveliotou, M. S. Briggs, & G. J. Fishman (New York: AIP), 133

Briggs, M.S., et al. 1999, *ApJ*, in press

Briggs, M.S., et al. 1999, *ApJ*, submitted [astro-ph/9903247]

Crider, A., et al. 1997, *ApJ*, 497, L39

Dingus, B. L. 1995, *Ap&SS*, 231(1), 187

Fishman, G. J., et al., 1994, *ApJS*, 92, 229 (BATSE 1B Catalog)

Ford, L. A., et al. 1995, *ApJ*, 439, 307

Goodman, J. 1986, *ApJ*, 308, L47

Hanlon, L. O., Bennet, K., Williams, O. R., Winkler, C., & Preece, R. D. 1995, *Ap&SS*, 231(1), 157

Harris, M .J., & Share, G. H. 1998, *ApJ*, 494, 724

Hurley, K., et al. 1994, *Nature*, 372, 652

Katz, J. I. 1994a, *ApJ*, 432, L107

Kippen, R. M. et al. 1995, in “Gamma-Ray Bursts, 3rd Huntsville Symposium”, ed. C. Kouveliotou, M. S. Briggs, & G. J. Fishman (New York: AIP), 197.

Liang, E. P., & Kargatis, V. E. 1996, *Nature*, 381, 49

Lloyd, N. M., & Petrosian, V. 1999, *ApJ*, 511, 550

Mallozzi, R. S., Pendleton, G. N., Paciesas, W. S., Briggs, M. S., Preece, R. D., Meegan, C. A., & Fishman, G. J. 1995, *ApJ*, 454, 597

Mallozzi, R. S., Pendleton, G. N., Paciesas, W. S., Preece, R. D., & Briggs, M. S. 1998, in “Gamma-Ray Bursts, 4th Huntsville Symposium”, ed. C. A. Meegan, R. D. Preece, & T. Koshut (New York: AIP), 273.

Mallozzi, R. S., et al. 1999, *ApJ*, in preparation

Matz, S. M., et al. 1985, ApJ, 288, L37

Meegan, C. A., et al. 1996, ApJS, 106, 65 (BATSE 3B Catalog)

Mészáros, P. & Rees, M. J. 1993, ApJ, 405, 278

Paciesas, W. S., et al. 1999, ApJS, submitted (BATSE 4B Catalog)

Pendleton, G. N., et al. 1994, ApJ, 431, 416

Pendleton, G. N., et al. 1995, NIMSA, 364, 567

Pendleton, G. N., et al. 1997, ApJ, 489, 175

Pendleton, G. N., et al. 1999, ApJ, in preparation

Preece, R. D., et al. 1996, ApJ, 473, 310

Preece, R. D., et al. 1998, ApJ, 496, 849

Preece, R. D., et al. 1998, ApJ, 506, L23

Rees, M. J., & Mészáros, P. 1994, ApJ, 430, L93

Ryde, F., & Svensson, R. 1998, in the proc. of the 3rd INTEGRAL Workshop: The Extreme Universe

Strohmayer, T. E., Fenimore, E. E., Murakami, T., & Yoshida, A. 1997, ApJ, 500, 873

Tavani, M. 1995, Ap&SS, 231(1), 181